

Spike-EVPR: Deep Spiking Residual Network with Cross-Representation Aggregation for Event-Based Visual Place Recognition

Chenming Hu , Zheng Fang , *Member, IEEE*, Kuanxu Hou , Delei Kong ,
Graduate Student Member, IEEE, Junjie Jiang , Hao Zhuang , Mingyuan Sun , Xinjie Huang 

Abstract—Event cameras have been successfully applied to visual place recognition (VPR) tasks by using deep artificial neural networks (ANNs) in recent years. However, previously proposed deep ANN architectures are often unable to harness the abundant temporal information presented in event streams. In contrast, deep spiking networks exhibit more intricate spatio-temporal dynamics and are inherently well-suited to process sparse asynchronous event streams. Unfortunately, directly inputting temporal-dense event volumes into the spiking network introduces excessive time steps, resulting in prohibitively high training costs for large-scale VPR tasks. To address the aforementioned issues, we propose a novel deep spiking network architecture called Spike-EVPR for event-based VPR tasks. First, we introduce two novel event representations tailored for SNN to fully exploit the spatio-temporal information from the event streams, and reduce the video memory occupation during training as much as possible. Then, to exploit the full potential of these two representations, we construct a Bifurcated Spike Residual Encoder (BSR-Encoder) with powerful representational capabilities to better extract the high-level features from the two event representations. Next, we introduce a Shared & Specific Descriptor Extractor (SSD-Extractor). This module is designed to extract features shared between the two representations and features specific to each. Finally, we propose a Cross-Descriptor Aggregation Module (CDA-Module) that fuses the above three features to generate a refined, robust global descriptor of the scene. Our experimental results indicate the superior performance of our Spike-EVPR compared to several existing EVPR pipelines on Brisbane-Event-VPR and DDD20 datasets, with the average Recall@1 increased by 7.61% on Brisbane-Event-VPR and 13.20% on DDD20.

Index Terms—Visual place recognition (VPR), event camera, deep spiking residual network, cross-representation aggregation, weakly supervised learning.

I. INTRODUCTION

Manuscript received: February 15, 2024. This work was supported in part by the National Natural Science Foundation of China under Grants 62073066 and U20A20197, in part by the Fundamental Research Funds for the Central Universities under Grant N2226001, in part by 111 Project under Grant B16009, and in part by the Intel Neuromorphic Research Community (INRC) Grant Award (RV2.137.Fang). (*Corresponding author: Zheng Fang.*)

Chenming Hu, Zheng Fang, Kuanxu Hou, Delei Kong, Junjie Jiang, Hao Zhuang, Mingyuan Sun, and Xinjie Huang are with the Faculty of Robot Science and Engineering, Northeastern University, Shenyang, China (e-mail: hucm6108@gmail.com, fangzheng@mail.neu.edu.cn, houkuanxu95@gmail.com, kong.delei.neu@gmail.com, jianggalaxypur-sue@gmail.com, howechong9@gmail.com, mingyuansun20@gmail.com, gg.xinjie.huang@gmail.com).

Digital Object Identifier (DOI): see top of this page.

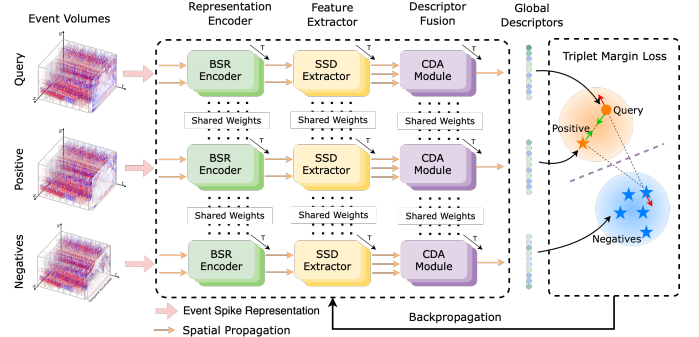


Fig. 1. Overview of Our Spike-EVPR Pipeline. Firstly our pipeline processes the event volumes into two distinct spike representations. Then after going through the three proposed modules, we can get a refined robust global descriptor for matching. See Fig. 2 for a more detailed pipeline.

EVENT cameras, also known as dynamic vision sensors (DVS), are neuromorphic cameras designed to mimic the functionality of the human eye [1]–[5]. Unlike traditional cameras (otherwise known as frame cameras), which accumulate light intensity and produce image frames within a fixed exposure time, event cameras output a continuous stream of asynchronous events. The unique signal-triggering mechanism of event cameras enables them to possess some remarkable attributes, such as ultra-high temporal resolution and ultra-wide dynamic range. Previous works have shown that these advantages can effectively alleviate some limitations of traditional cameras, such as image quality degradation caused by motion blur in high-speed motion scenes, and difficulty in capturing the texture features of scenes in low-light environments [6], [7]. This makes the adoption of event cameras for visual place recognition (VPR) become popular.

VPR stands as a critical subtask for the autonomous navigation of mobile robots [8]–[11]. Its primary objective is to aid the robot in repositioning itself within a known mapped environment. It involves working with a database that contains visual data, such as RGB frames, from various locations within the environment. When provided with a query, the VPR system searches for the corresponding frame with location information in the database, enabling the robot to achieve localization and closed-loop detection (LCD) within a GPS-denied environment. In recent years, significant research efforts have been devoted to leveraging the advantages of event cameras to create VPR pipelines, known as event-based VPR (EVPR) [7], [12]–[16]. Although there have been various efforts for EVPR, most

works still rely on convolutional networks and fail to leverage the dense timestamps offered by the event streams [7], [12]–[15].

In contrast, spiking neural networks (SNNs) are more suitable for processing data with rich timestamps, and the asynchronous triggering paradigm of event cameras is naturally suitable for SNNs [17]. SNNs are regarded as a new generation of neural networks known for their exceptional biological fidelity, asynchronous event-driven, and low power consumption [18]. Unlike artificial neural networks (ANNs) that use floating-point numbers, SNNs communicate between spiking neurons via spike signals, exhibiting more intricate spatio-temporal dynamics. When processing event data, event-driven SNNs demonstrate greater suitability, faster processing, and reduced latency than ANNs. For certain small-scale tasks, such as gesture recognition, SNNs have demonstrated advantages in both accuracy and power consumption [19], [20]. This provides a new possibility for further improving the performance of the EVPR pipeline.

Currently, there are two primary challenges in utilizing SNNs for event data processing in EVPR: (1) Event streams have rich timestamps, but it is difficult to feed temporal-dense event tensors directly into SNNs. Because it will have too many time steps and lead to too high network training costs. Moreover, event data is highly spatially sparse at a single time step, which hinders the SNN’s capacity to encode spatial neighborhood information of the scene. For EVPR tasks, it is difficult for a single representation to make full use of event data. Therefore, multiple representations may need to be designed. Thus, how to compress event data to generate representations that fit the SNN is an issue that needs to be solved. (2) For EVPR with complex scenes, shallow SNNs may not be competent, and deep spiking networks need to be designed to obtain robust global feature descriptors of scenes. Thus, upon acquiring compact spike event representations, the subsequent challenge is how to construct a deep spiking network to efficiently fuse multiple representations and fully exploit discriminative features.

To deal with the aforementioned challenges, we propose Spike-EVPR¹, a novel descriptor extractor pipeline for large-scale EVPR tasks based on deep spiking residual network architecture with cross-representation aggregation, as shown in Fig. 1. It can effectively fuse two spike representations to obtain a more robust scene descriptor for better EVPR performance while controlling the SNN training cost. To our knowledge, this is the first end-to-end directly-trained SNN-based EVPR pipeline that achieves the SOTA EVPR performance. In summary, the main contributions of this article can be summarized as follows:

- Aiming at the EVPR task, we first propose two spike representations, namely the Multi-Channel Spike Tensor (MCS-Tensor) and Time-Surface Spike Tensor (TSS-Tensor), to reduce the SNN training cost. They can retain more scene information compared to a single representa-

tion, thereby enabling the network to extract more robust visual features.

- We design a Bifurcated Spike Residual Encoder (BSR-Encoder) with multiple spike residual blocks to extract the specific spike features of each spike representation. And, in triplet contrastive learning, we introduce a detailed derivation of the spatio-temporal back-propagation (STBP) for LIF-based BSR-Encoder.
- We propose a Shared & Specific Descriptor Extractor (SSD-Extractor) and a Cross-Descriptor Aggregation Module (CDA-Module) to effectively excavate discriminative features and integrate them. The former can obtain multiple sub-descriptors with distinct characteristics by splitting and reassembling the two spike features from the BSR-Encoder. The latter automatically learns the weights of different sub-descriptors and aggregates them into a more refined global descriptor.
- We make a comprehensive comparison between our Spike-EVPR and existing SOTA EVPR methods on Brisbane-Event-VPR and DDD20 datasets to demonstrate the advanced performance of our method, in which the average value of different sequence Recall@1 on Brisbane-Event-VPR is increased by 7.61%, and the average value of different sequence Recall@1 on DDD20 is increased by 13.20%. We conduct ablation studies on each network component to comprehensively demonstrate the compactness of our Spike-EVPR pipeline.

The rest of this article is organized as follows. First, Section II reviews related works on VPR and SNN. Then, Section III describes the overall network pipeline of our Spike-EVPR and introduces two SNN-tailored event representations, BSR-Encoder, SSD-Extractor, and CDA-Module in detail. Next, the experimental results of our Spike-EVPR on Brisbane-Event-VPR and DDD20 datasets are presented in Section IV. Finally, Section V concludes this article.

II. RELATED WORK

A. Visual Place Recognition (VPR)

1) *Frame-based VPR*: Numerous frame-based algorithms for Visual Place Recognition (VPR) have been presented in the past. Previous works primarily relied on manually designed methods for feature extraction [21]–[23]. These methods generated global descriptors by constructing bag-of-word vectors [24] based on local feature points. With the development of deep learning, Arandjelovic et al. [25] proposed a feature coding network that can be trained end-to-end, eliminating the need for clustering centers, which were traditionally required by VLAD [26]. Subsequently, Yu et al. [27] introduced spatial pyramids to enhance the ability of the NetVLAD model to capture feature information at different spatial scales. Moreover, Hausler et al. [28] achieved superior results compared to NetVLAD by generating global descriptors for the entire image and then utilizing local patches to produce further refined local descriptors through fine-tuning. In recent years, benefit of large-scale training on VPR-specific datasets, several advanced algorithms have emerged in the field. For instance, CosPlace [29] trained its VPR model using a dense, large-scale

¹Supplementary Material: An accompanying video for this work is available at https://youtu.be/v8ch0aFDm_k.

dataset called San Francisco XL, originally designed for image classification tasks, which includes a staggering 40 million images. MixVPR [30] trained on the GSV-Cities dataset [31], a highly accurate dataset of 560,000 images representing 67,000 distinct locations. The most recent SOTA method, AnyLoc [32], leverages a large-scale visual model, DINOv2 [33], for feature extraction and employs unsupervised VLAD for feature aggregation, achieving the current SOTA performance without specific training.

2) *Event-based VPR (EVPR)*: Due to the potential of event cameras, several notable approaches have emerged in the field of VPR. Tobias et al. [12] proposed Ensemble-Event-VPR, which utilizes reconstructed image sequences from the event streams within multiple time windows to obtain multiple descriptors and integrates them using NetVLAD. Lee et al. [13] proposed EventVLAD, which incorporates edge images generated from the event streams into NetVLAD to produce a descriptor. Kong et al. [14] proposed Event-VPR, which first characterizes the event streams, and then feeds it into the deep residual network and VLAD layer for triplet learning. Tobias et al. [16] proposed Sparse-Event-VPR, which uses only a few sparse key events to obtain descriptors, making the algorithm lighter in terms of computational load, albeit with only marginal performance improvements. Huang et al. [15] proposed VEFNet, which merges frames and events through cross-attention and self-attention networks. However, this approach has shown only modest enhancements in performance. Lastly, Hou et al. [7] proposed FE-Fusion-VPR, which combined frames and events through dual-stream feature extractors, multi-scale networks, and reweighted networks, validated the complementary nature of the two visual data sources on challenging data samples. However, existing EVPR methods rely solely on CNNs for feature extraction and do not fully harness the rich event temporal information.

B. Spiking Neural Network

Currently, two mainstream types of neural networks are ANNs and SNNs. SNNs distinguish themselves from traditional ANNs by processing 1-bit spike events, encoding information in discrete spike trains instead of continuous real values. However, SNNs can be challenging to train because of their discrete nature. Currently, the two most prominent methods for training deep spiking neural networks are the ANN-to-SNN method [34]–[37] and the surrogate gradient method [38]. However, the converted SNNs using the ANN-to-SNN method may require more time steps to attain results comparable to those achieved by ANNs. The surrogate gradient method enables the direct training of SNNs through backpropagation, using continuous gradient approximations mapped into the non-differentiable spike domain. Compared to the ANN-to-SNN method, surrogate gradient learning is more resource-efficient as it uses continuous gradient approximations instead of discrete spike simulations. They can also be trained at various time steps, offering greater flexibility and scalability. The inherent sparse and asynchronous nature of event cameras aligns well with SNNs, making them increasingly popular among researchers who seek to address

conventional problems in computer vision in conjunction with event cameras. Applications include optical flow prediction [39], motion segmentation [40], object detection [41], depth estimation [42], and more. Recently, there have been efforts to utilize spiking neural networks for EVPR tasks. Lee et al. [43] use an ANN-to-SNN network to reconstruct edge images from event data and then feed these images into NetVLAD for feature extraction. This work predominantly relies on the ANN-to-SNN method for image reconstruction, with traditional ANN algorithms still being used for feature extraction. However, this approach does not fully leverage the spatio-temporal properties of SNNs in feature extraction, leaving room for further exploration and optimization of the combination of these techniques.

III. METHODOLOGY

A. The Overall Architecture

The detailed illustration of our proposed Spike-EVPR pipeline is shown in Fig. 2. First of all, our pipeline processes the event volumes into two event spike representations, namely Multi-Channel Spike Tensor (MCS-Tensor) and Time-Surface Spike Tensor (TSS-Tensor), to reduce the training cost and retain more scene information. Subsequently, we introduce three sub-modules to comprehensively extract visual information from event data for aggregating a robust global descriptor. Firstly, a Bifurcated Spike Residual Encoder (BSR-Encoder) is designed based on deep spiking residual blocks to extract the spike feature maps of the above two representations. Then, we propose a Shared & Specific Descriptor Extractor (SSD-Extractor). By splitting and recombining the spike feature maps from the two representations, we obtain feature maps with distinct characteristics and their corresponding sub-descriptors. Finally, a Cross-Descriptor Aggregation Module (CDA-Module) is proposed to fuse the multiple sub-descriptors generated by SSD-Extractor. It can automatically learn the weights of different sub-descriptors and aggregate them into a refined global descriptor. Importantly, the entire pipeline is trained end-to-end using weakly supervised triplet contrastive learning.

B. Leaky Integrate-and-Fire (LIF) Neurons

Let's start with a brief description of the spiking neurons we used. In SNNs, spiking neurons are specifically designed to mimic the dynamics of biological neurons, drawing inspiration from the field of neuroscience. In our Spike-EVPR, the Leaky Integrate-and-Fire (LIF) neuron [44] is predominantly used, which is also a commonly employed spiking neuron in SNNs. LIF neurons can integrate spike trains into the membrane voltage. The membrane voltage undergoes attenuation through a decay coefficient of the voltage δ_n and emits a spike when it surpasses a spike-triggered threshold u_{th} . The iteration update equation illustrating the internal structure of the LIF layer, which demonstrates these phases, is presented as follows:

$$\begin{aligned} U_n^t &= \delta_n U_n^{t-1} g(O_n^{t-1}) + W_n O_{n-1}^t \\ O_n^t &= h(U_n^t) \end{aligned} \quad (1)$$

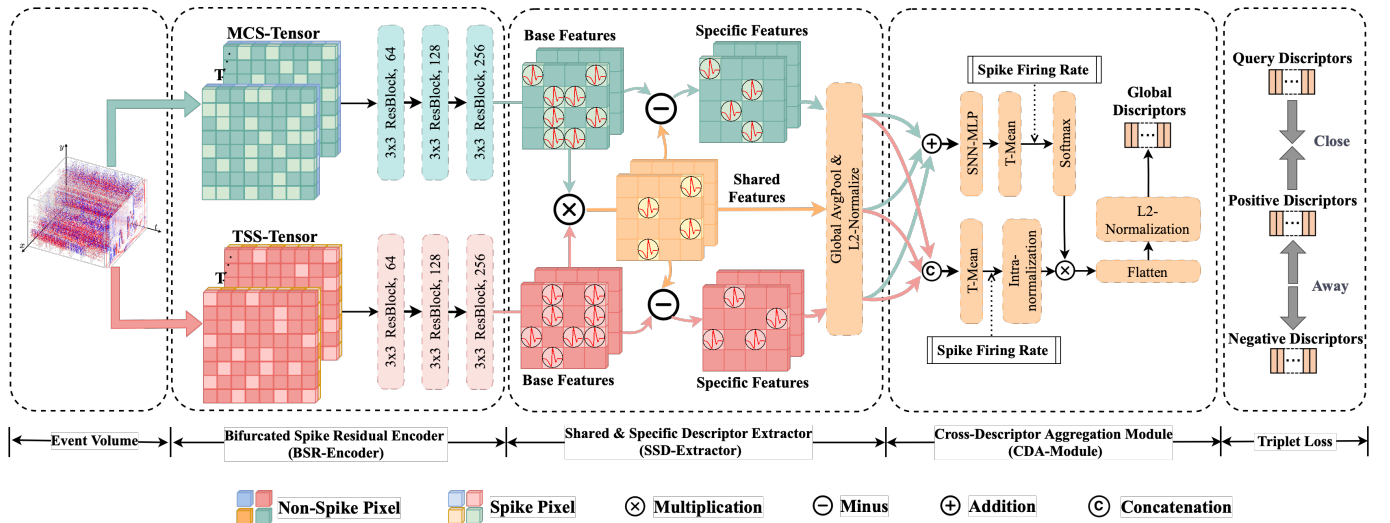


Fig. 2. Detailed illustration of the proposed Spike-EVPR pipeline. Firstly, the event volume is converted into MCS-Tensor and TSS-Tensor as input respectively. Then, they are sent to the Bifurcated Spike Residual Encoder (BSR-Encoder) module to obtain two initial feature maps. After that, these two feature maps are aggregated into three diverse sub-descriptors using Shared & Specific Descriptor Extractor (SSD-Extractor). Finally, these sub-descriptors are fed into the Cross-Descriptor Aggregation Module (CDA-Module) to obtain the final refined global descriptor for matching.

where $t \in [1, T]$ denotes the discrete time, U_n^t is the membrane voltage, δ_n is the decay coefficient of the voltage. $g(O_n^{t-1}) = 1 - O_n^{t-1}$ is the reset gate. $h(U_n^t) = H(U_n^t - u_{th,n})$ is the fire gate, if the membrane voltage U_n^t exceeds the spike-triggered threshold $u_{th,n}$, the output spike train O_n^t is setted as 1.

C. SNN-Tailored Event Representations

Event streams exhibit rich timestamps. However, for EVPR tasks, given the current computational capabilities of computer hardware, the temporal information within the event streams is overly dense. Directly processing the raw event streams leads to significant training costs. It is necessary to compress the event data on the time steps. Meanwhile, the event data at each time step is very sparse in the spatial neighborhood. This inadequacy hinders the ability of the SNNs to learn the spatial information of the scene effectively. To address this, we introduce two event spike representations, which are specifically tailored for SNNs and designed for EVPR tasks: the Multi-Channel Spike Tensor (MCS-Tensor) and the Time-Surface Spike Tensor (TSS-Tensor).

1) *Multi-Channel Spike Tensor (MCS-Tensor)*: As shown in Fig. 3, Multi-Channel Spike Tensor (MCS-Tensor) is a learnable spike representation, that reduces network training costs by mapping sparse event data to the appropriate time-step through the network. As shown in Eq. (3), the fundamental core behind MCS-Tensor is to encode event timestamps using a Spiking Multi-Layer Perceptron (SMLP) denoted as $f_{SMLP}(\cdot)$:

$$f_{SMLP}(\cdot) = f_{LIF,2}(f_{FC,2}(f_{LIF,1}(f_{FC,1}(E)))) \quad (2)$$

where $f_{FC,1}(\cdot)$ and $f_{FC,2}(\cdot)$ are the two fully connected layers, respectively. Each fully connected layer is associated with the LIF neuron layer $f_{LIF}(\cdot)$ for the spike coding of event timestamps. This encoding transforms the event timestamps into appropriate time step and yields a spiking tensor with dimensions $\mathbb{R}^{T \times C \times H \times W}$, which serves as input to the subsequent feature extraction network. The MCS-Tensor is defined as follows:

$$\begin{aligned} \mathcal{V}_+(x', y', t') &= \sum_{e_i \in E_+} p_i \delta(x' - x_i, y' - y_i) f_{SMLP}(t' - t_i^*), \\ \mathcal{V}_-(x', y', t') &= \sum_{e_i \in E_-} |p_i| \delta(x' - x_i, y' - y_i) f_{SMLP}(t' - t_i^*), \end{aligned} \quad (3)$$

where x', y', t' are the encoded spiking tensor space-time coordinates. Among them, $x' = 0, 1, \dots, W - 1, y' = 0, 1, \dots, H - 1, t' = 0, 1, \dots, T - 1$, where (W, H) is the spatial resolution and T is the time step. $t_i^* = (T - 1) \frac{(t_i - t_1)}{(t_{last} - t_1)}$ means event timestamps are normalized and distributed to the corresponding time-steps. $f_{SMLP}(\cdot)$ is a kernel function consisting of two spiking fully connected layers, defined by Eq. (2).

2) *Time-Surface Spike Tensor (TSS-Tensor)*: To enable the network to capture more spatial information about the scene, we propose a Time-Surface Spike Tensor (TSS-Tensor) which efficiently encodes the spatiotemporal structure information of the event stream and has invariance to the lighting changes of the scene. This restoration of spatial information is achieved by mapping sparse pixels in the whole event volume to the event frame. Since SNNs require discrete spike trains as input, we spike-coded the event frame using the Bernoulli distribution to generate the spike tensor fitted for SNNs. We use the Time-Surface (TS) map [45] as the event frame, where each pixel stores information about the time of the last event at that pixel using the exponential decay kernel, effectively encoding the temporal information of events. The TS is defined as follows:

$$\begin{aligned} \tilde{\mathcal{T}}_+(x', y') &= \exp\left(-\frac{t_{end} - t_{last,+}(x', y')}{\eta}\right), \\ \tilde{\mathcal{T}}_-(x', y') &= \exp\left(-\frac{t_{end} - t_{last,-}(x', y')}{\eta}\right), \end{aligned} \quad (4)$$

where t_{end} represents the termination moment of the event volume. $t_{last,\pm}(x', y')$ represents the timestamps of the last positive and negative events at each frame pixel (x', y') , respectively. The parameter η is the decay rate. We employ the Bernoulli coding to transform the event frame which contains continuous floating-point values into discrete spike trains. As

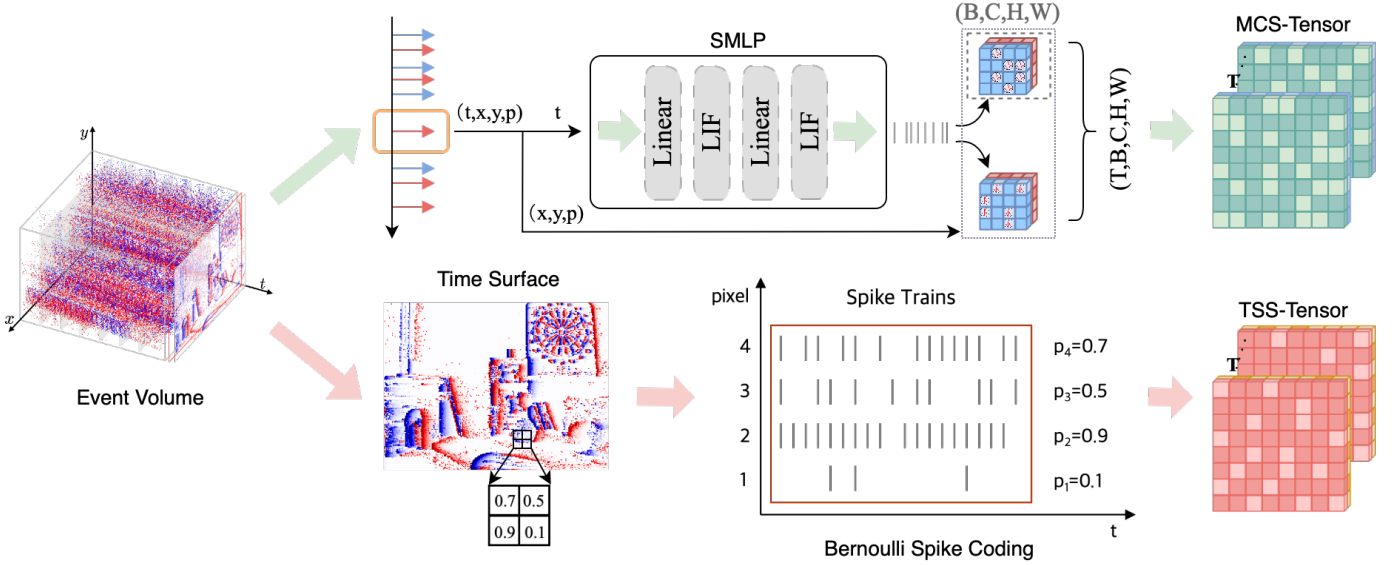


Fig. 3. Detailed illustration of our MCS-Tensor and TSS-Tensor. Upper part is the illustration of the proposed MCS-Tensor. Firstly, We first split the event streams into event volumes. Secondly, the events of the event volume are input one by one into the SMLP layer consisting of two fully connected spiking layers with LIF neurons. Finally, we obtain a MCS-Tensor. Downer part is the illustration of the proposed TSS-Tensor. Event streams are processed first as time-surface. Then, we spike-coded the time-surface using the Bernoulli distribution to generate the spike tensor fitted for SNNs.

illustrated in Eq. (5), we assume that the spike firing rate of the encoded spike trains is correlated with the floating-point value of the TS map in each pixel. By mapping the pixel value $\tilde{\mathcal{T}}(x', y')$ from the TS map to the probability parameter $p_{x', y'}$ of the Bernoulli distribution and repeatedly sampling the value over T time steps, we can restore the time information of event frame into spike trains which initially compressed as floating-point values. The map from the TS map to the spike tensor can be summarized as follows:

$$\mathcal{T}_{\pm}(x', y', t') \sim \mathcal{B}(\tilde{\mathcal{T}}_{\pm}, p_{x', y'}, T), \quad (5)$$

where $\mathcal{B}(\cdot)$ is the Bernoulli distribution in regard to the TS map. $p_{x', y'}$ denotes the probability parameter of the Bernoulli distribution at event frame coordinate (x', y') . T denotes the time step which is also the number of repetitions of Bernoulli coding.

D. Deep Spiking Network Architecture

1) Bifurcated Spike Residual Encoder (BSR-Encoder):

Based on the dual SNN-tailored event representations discussed above, we use a spike residual network with powerful feature extraction capabilities for feature extraction. As shown in Fig. 2, our Bifurcated Spike Residual Encoder (BSR-Encoder) extracts the initial feature maps of two event spike representations through a dual-stream deep spiking residual network, which can be summarized as follows:

$$\begin{aligned} \mathbf{M}_{\text{MCS}}, \mathbf{M}_{\text{TSS}} &= \mathbf{f}_{\text{BSR-Encoder}}(\mathbf{V}_{\pm}, \mathcal{T}_{\pm}) \\ &= \mathbf{f}_{\text{SR13-MCS}}(\mathbf{V}_{\pm}), \mathbf{f}_{\text{SR13-TSS}}(\mathcal{T}_{\pm}), \end{aligned} \quad (6)$$

where $\mathbf{f}_{\text{SR13-MCS}}(\cdot)$ and $\mathbf{f}_{\text{SR13-TSS}}(\cdot)$ are two 13-layer spike residual feature extraction networks, respectively. \mathbf{V}_{\pm} and \mathcal{T}_{\pm} are two-stream SNN-tailored event representations introduced in last section. $\mathbf{M}_{\text{MCS}}, \mathbf{M}_{\text{TSS}} \in \mathbb{B}^{T \times C \times H \times W}$ are the initial feature maps of the two representations which are generated by the BSR-Encoder. We employ spike residual blocks to construct our BSR-Encoder, as depicted in Fig. 4 and Eq. (7):

$$\mathbf{F}_n(\cdot) = \mathbf{f}_{\text{BN}, n}(\mathbf{f}_{\text{Conv}, n}(\mathbf{f}_{\text{LIF1}, 1}(\mathbf{f}_{\text{BN}, n}(\mathbf{f}_{\text{Conv}, n}(\cdot))))), \quad (7)$$

$\mathbf{O}_n^t = \mathbf{f}_{\text{LIF2}, n}(\mathbf{F}_n(\mathbf{O}_{n-1}^t) + \mathbf{O}_{n-1}^t)$, where $\mathbf{F}_n(\cdot)$ consists of 3×3 convolutional layer $\mathbf{f}_{\text{Conv}, n}(\cdot)$, batch-normalization layer $\mathbf{f}_{\text{BN}, n}(\cdot)$ and LIF neuron layer $\mathbf{f}_{\text{LIF}, n}(\cdot)$. \mathbf{O}_{n-1}^t and \mathbf{O}_n^t are the input spike trains and output spike trains, respectively. The spike residual network combines the attributes of the residual network and the spiking network, enabling it to efficiently capture the temporal information of event streams, mitigate gradient vanishing and explosion issues, and enhance the stability of the deep spiking network.

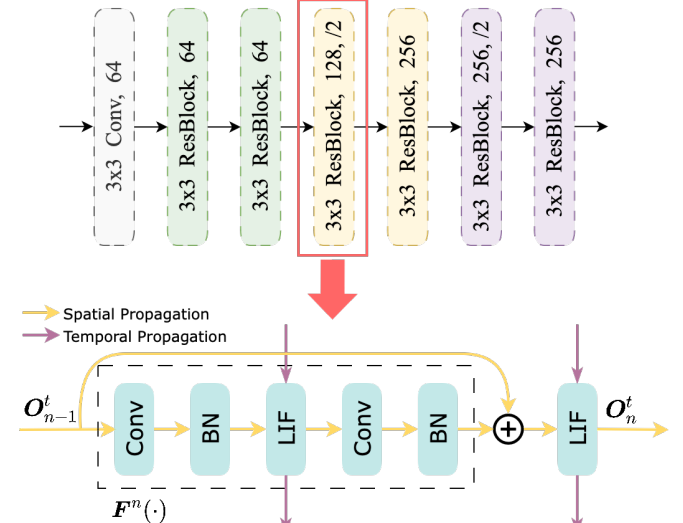


Fig. 4. The structure of the SR13 in Bifurcated Spike Residual Encoder (BSR-Encoder), and a detailed diagram about the basic resblock of BSR-Encoder.

2) Shared & Specific Descriptor Extractor (SSD-Extractor):

After getting the initial feature maps of the proposed two spike representations, we then design a Shared and Specific Descriptor Extractor (SSD-Extractor) to obtain the shared and specific sub-descriptors that take account of the characteristics of the BSR-Encoder's output spike feature maps. As illustrated in Fig. 2, given that the initial spike feature maps contain

values of only 1 and 0, we can identify the shared feature map in the two spike feature maps by performing element-wise multiplication. The specific feature maps for the two representations are then obtained by subtracting the shared feature map from their respective initial feature map. These operations can be summarized as follows:

$$\begin{aligned} \mathbf{X}_1 &= \mathbf{M}_{\text{MCS}} \otimes \mathbf{M}_{\text{TSS}}, \\ \mathbf{X}_2 &= \mathbf{M}_{\text{MCS}} \ominus \mathbf{X}_1, \\ \mathbf{X}_3 &= \mathbf{M}_{\text{TSS}} \ominus \mathbf{X}_1, \end{aligned} \quad (8)$$

where $\mathbf{M}_{\text{MCS}}, \mathbf{M}_{\text{TSS}} \in \mathbb{B}^{\text{T} \times \text{C} \times \text{H} \times \text{W}}$ denote the feature maps of MCS-Tensor \mathcal{V} and TSS-Tensor \mathcal{T} , respectively. $\mathbf{X}_1 \in \mathbb{B}^{\text{T} \times \text{C} \times \text{H} \times \text{W}}$ denotes the shared feature map of the two representations. $\mathbf{X}_2, \mathbf{X}_3 \in \mathbb{B}^{\text{T} \times \text{C} \times \text{H} \times \text{W}}$ denote the specific feature maps of MCS-Tensor and TSS-Tensor, respectively. \otimes and \ominus are element-wise multiplication and subtraction, respectively. Following that, we apply global average pooling (GAP) and L2 normalization on the shared feature map \mathbf{X}_1 and specific feature maps $\mathbf{X}_2, \mathbf{X}_3$ from two event representations, to obtain the three sub-descriptors $\mathbf{D}_1, \mathbf{D}_2, \mathbf{D}_3 \in \mathbb{R}^{\text{T} \times \text{C}}$, which are expressed as follows:

$$\mathbf{D}_1, \mathbf{D}_2, \mathbf{D}_3 = \mathbf{f}_{\text{L2-norm}}(\mathbf{f}_{\text{GAP}}(\mathbf{X}_1, \mathbf{X}_2, \mathbf{X}_3)), \quad (9)$$

where $\mathbf{f}_{\text{GAP}}(\cdot)$ and $\mathbf{f}_{\text{L2-norm}}(\cdot)$ represent global average pooling and L2-normalization, respectively. Among these sub-descriptors, \mathbf{D}_1 incorporates shared information from both representations, whereas $\mathbf{D}_2, \mathbf{D}_3$ encompass specific information from each representation, respectively. Since the obtained three sub-descriptors contain shared and specific information of the two spike representations, they can provide abundant and diverse information for the CDA-Module to get a more robust descriptor.

3) Cross-Descriptor Aggregation Module (CDA-Module):

In the SSD-Extractor, we obtain specific and shared feature sub-descriptors from the proposed two representations. To better fuse these sub-descriptors, we introduce the Cross-Descriptor Aggregation Module (CDA-Module) $\mathbf{f}_{\text{CDA-Module}}(\cdot)$ to autonomously learn and selectively emphasize vital information from different descriptors, aimed at deriving a robust global descriptor:

$$\tilde{\mathbf{D}} = \mathbf{f}_{\text{CDA-Module}}(\mathbf{D}_1, \mathbf{D}_2, \mathbf{D}_3). \quad (10)$$

Firstly, we learn the weights of the three sub-descriptors (shared and specific descriptors), as illustrated in Eq. (11). Initially, the three diverse sub-descriptors $\mathbf{D}_1, \mathbf{D}_2, \mathbf{D}_3$ are element-wise summed to obtain $\mathbf{D}_{\text{add}} \in \mathbb{R}^{\text{T} \times \text{C}}$. Subsequently, the sub-descriptor $\mathbf{D}'_{\text{add}} \in \mathbb{R}^{\text{T} \times 3}$ is obtained through a SMLP, composed of two fully connected layers with 256 neurons in the input layer (corresponding to the length of descriptors), 64 neurons in the middle hidden layer, and 3 neurons in the output layer (corresponding to the number of sub-descriptors). Afterward, the sub-descriptors are averaged along the temporal dimension to determine the spike firing rate. Finally, the obtained spike firing rate undergoes the Soft-Max function to derive the weight of each basic descriptor $\mathbf{w} \in \mathbb{R}^3$, which are expressed as follows:

$$\begin{aligned} \mathbf{D}_{\text{add}} &= \mathbf{D}_1 \oplus \mathbf{D}_2 \oplus \mathbf{D}_3, \\ \mathbf{D}'_{\text{add}} &= \mathbf{f}_{\text{FC},2}(\mathbf{f}_{\text{LIF}}(\mathbf{f}_{\text{FC},1}(\mathbf{D}_{\text{add}}))), \\ \mathbf{w} &= \mathbf{f}_{\text{SM}}(\mathbf{f}_{\text{Mean}}(\mathbf{D}'_{\text{add}})) \end{aligned} \quad (11)$$

where $\mathbf{D}_1, \mathbf{D}_2$, and \mathbf{D}_3 are the shared sub-descriptor and specific sub-descriptors for two representations, respectively. $\mathbf{D}_{\text{add}} \in \mathbb{R}^{\text{T} \times \text{C}}$ represents the sub-descriptor after element-wise addition of the three sub-descriptors. $\mathbf{f}_{\text{FC},1}(\cdot) : \mathbb{R}^{\text{T} \times 256 \times 1} \rightarrow \mathbb{R}^{\text{T} \times \text{M} \times 1}$ and $\mathbf{f}_{\text{FC},2}(\cdot) : \mathbb{R}^{\text{T} \times \text{M} \times 1} \rightarrow \mathbb{R}^{\text{T} \times 3 \times 1}$ are two kinds of fully connected layers. $\text{M} = 64$ is the transformation length of the global representation in the hidden layer. $\mathbf{f}_{\text{Mean}}(\cdot) : \mathbb{R}^{\text{T} \times 3 \times 1} \rightarrow \mathbb{R}^{3 \times 1}$ indicates the average spike firing rate of the sub-descriptors averaged along the temporal dimension. $\mathbf{f}_{\text{SM}}(\cdot)$ means the Soft-Max operation which makes the weights of these three descriptors mutually balanced. Secondly, the three sub-descriptors $\mathbf{D}_1, \mathbf{D}_2, \mathbf{D}_3 \in \mathbb{R}^{\text{T} \times \text{C}}$ are concatenated in a new dimension to obtain $\mathbf{D}_{\text{concat}} \in \mathbb{R}^{\text{T} \times 3 \times \text{C}}$. Then, the average spike firing rate of the sub-descriptor is obtained by averaging the T dimension to get $\mathbf{D}'_{\text{concat}} \in \mathbb{R}^{3 \times \text{C}}$. Normalization is then carried out independently within each descriptor in the C dimension, which is expressed as follows:

$$\mathbf{D}_{\text{concat}} = \left\| \bigg|_{i=1}^3 (\mathbf{D}_i), \right. \quad (12)$$

$$\mathbf{D}'_{\text{concat}} = \mathbf{f}_{\text{Intra-norm}}(\mathbf{f}_{\text{Mean}}(\mathbf{D}_{\text{concat}})),$$

where $\left\| \bigg|_{i=1}^3 (\cdot)$ denotes the concatenation operation, and $\mathbf{D}_{\text{concat}} \in \mathbb{R}^{\text{T} \times 3 \times \text{C}}$ is the new spike tensor after concatenation operation. $\mathbf{f}_{\text{Mean}}(\cdot) : \mathbb{R}^{\text{T} \times 3 \times \text{C}} \rightarrow \mathbb{R}^{3 \times \text{C}}$ denotes the spike average firing rate of the spike tensor. $\mathbf{f}_{\text{Intra-norm}}(\cdot)$ is an Intra-normalization operation. Finally, we multiply the concatenated descriptor $\mathbf{D}'_{\text{concat}}$ with the weight descriptor \mathbf{w} . After flatten and L2-normalize operation, the final refined descriptor is obtained $\mathbf{D}' \in \mathbb{R}^{3\text{C}}$. The final global descriptor considers the diverse information harbored by the various sub-descriptors and their disparate contributions, enhancing the model's performance and generalization capabilities. The final global descriptor is computed as follows:

$$\tilde{\mathbf{D}} = \mathbf{f}_{\text{L2-norm}}(\mathbf{f}_{\text{Flatten}}(\mathbf{D}'_{\text{concat}} \otimes \mathbf{w})), \quad (13)$$

where $\mathbf{f}_{\text{Flatten}}(\cdot) : \mathbb{R}^{3 \times \text{C}} \rightarrow \mathbb{R}^{3\text{C}}$ is flatten operation and $\mathbf{f}_{\text{L2-norm}}(\cdot)$ is the L2-Normalization operation.

E. Weakly Supervised Training

1) *Triplet Contrastive Learning*: To train the proposed Spike-EVPR, we employ the triplet loss $\mathcal{L}_{\text{triplet}}$ introduced by [25] for weakly supervised training. After we get the embeddings of each scene, the objective of triplet loss is to build a representation space where the gap between pairs of the query and positive ($\mathbf{D}_{\text{q}}, \mathbf{D}_{\text{pos}}$) should be as small as possible and the gap between the query and hard negatives ($\mathbf{D}_{\text{q}}, \mathbf{D}_{\text{neg}}$) should be as big as possible. The weakly supervised triplet ranking loss we used is defined as follows:

$$\mathcal{L}_{\text{triplet}} = \max([\phi(\mathbf{D}_{\text{q}}, \mathbf{D}_{\text{pos}}) - \phi(\mathbf{D}_{\text{q}}, \mathbf{D}_{\text{neg}}) + m], 0), \quad (14)$$

where $\phi(\cdot, \cdot)$ is the Euclidean distance function and m is the margin.

2) *Spatio-Temporal Back Propagation for LIF-based BSR-Encoder*: As shown in Fig. 4, consider the BSR-Encoder with N ResBlocks, the iterative update equation of the first LIF neuron layer in each ResBlock $n \in [1, N]$ is given by:

$$\begin{aligned} \mathbf{U}_{n,1}^t &= \delta_{n,1} \mathbf{U}_{n,1}^{t-1} \mathbf{g}(\mathbf{O}_{n,1}^{t-1}) + \mathbf{W}_{n,1} \mathbf{O}_{n-1,2}^t, \\ \mathbf{O}_{n,1}^t &= \mathbf{h}(\mathbf{U}_{n,1}^t), \end{aligned} \quad (15)$$

The iterative update equation of the second LIF neuron layer in each ResBlock $n \in [1, N]$ is given by:

$$\begin{aligned} \mathbf{U}_{n,2}^t &= \delta_{n,2} \mathbf{U}_{n,2}^{t-1} \mathbf{g}(\mathbf{O}_{n,2}^{t-1}) + \mathbf{W}_{n,2} \mathbf{O}_{n,1}^t + \mathbf{O}_{n-1,2}^t, \\ \mathbf{O}_{n,2}^t &= \mathbf{h}(\mathbf{U}_{n,2}^t), \end{aligned} \quad (16)$$

Here, for the sake of the brevity of back-propagation derivation, we assume the $\mathbf{W}_{n,1}$ and $\mathbf{W}_{n,2}$ are the learnable parameters of the convolutional layer and the batch normalization layer in Eq. (7). According to Eq. (15) and Eq. (16), to obtain the derivation of $\mathcal{L}_{\text{triplet}}$ to the spikes $\mathbf{O}_{n,1}^t$ and $\mathbf{O}_{n,2}^t$, the voltages $\mathbf{U}_{n,1}^t$ and $\mathbf{U}_{n,2}^t$, it can be divided into the following four cases depending on the layer n and time t :

Case 1: At the time $t = T$ and the ResBlock $n = N$. In this case, only spatial derivatives exist. Concerning the second LIF neuron layer in the ResBlock, the derivation of $\mathcal{L}_{\text{triplet}}$ to $\mathbf{O}_{N,2}^T$ can be calculated by regular back-propagation:

$$\frac{\partial \mathcal{L}_{\text{triplet}}}{\partial \mathbf{O}_{N,2}^T} = \left. \frac{\partial \mathcal{L}_{\text{triplet}}}{\partial \mathbf{O}_{N,2}^T} \right|_{\text{spatial}} = \text{known values}, \quad (17)$$

$$\frac{\partial \mathcal{L}_{\text{triplet}}}{\partial \mathbf{U}_{N,2}^T} = \left. \frac{\partial \mathcal{L}_{\text{triplet}}}{\partial \mathbf{U}_{N,2}^T} \right|_{\text{spatial}} = \frac{\partial \mathcal{L}_{\text{triplet}}}{\partial \mathbf{O}_{N,2}^T} \dot{\mathbf{h}}(\mathbf{U}_{N,2}^T), \quad (18)$$

Concerning the first LIF neuron layer in the ResBlock:

$$\frac{\partial \mathcal{L}_{\text{triplet}}}{\partial \mathbf{O}_{N,1}^T} = \left. \frac{\partial \mathcal{L}_{\text{triplet}}}{\partial \mathbf{O}_{N,1}^T} \right|_{\text{spatial}} = \frac{\partial \mathcal{L}_{\text{triplet}}}{\partial \mathbf{U}_{N,2}^T} \mathbf{W}_{N,2}, \quad (19)$$

$$\frac{\partial \mathcal{L}_{\text{triplet}}}{\partial \mathbf{U}_{N,1}^T} = \left. \frac{\partial \mathcal{L}_{\text{triplet}}}{\partial \mathbf{U}_{N,1}^T} \right|_{\text{spatial}} = \frac{\partial \mathcal{L}_{\text{triplet}}}{\partial \mathbf{O}_{N,1}^T} \dot{\mathbf{h}}(\mathbf{U}_{N,1}^T). \quad (20)$$

Case 2: At the time $t = T$ and the middle ResBlock $n < N$. In this case, only spatial derivatives exist. Concerning the second LIF neuron layer in the ResBlock:

$$\begin{aligned} \frac{\partial \mathcal{L}_{\text{triplet}}}{\partial \mathbf{O}_{n,2}^T} &= \left. \frac{\partial \mathcal{L}_{\text{triplet}}}{\partial \mathbf{O}_{n,2}^T} \right|_{\text{spatial}} \\ &= \frac{\partial \mathcal{L}_{\text{triplet}}}{\partial \mathbf{U}_{n+1,1}^T} \mathbf{W}_{n,1} + \frac{\partial \mathcal{L}_{\text{triplet}}}{\partial \mathbf{U}_{n+1,2}^T}, \end{aligned} \quad (21)$$

$$\frac{\partial \mathcal{L}_{\text{triplet}}}{\partial \mathbf{U}_{n,2}^T} = \left. \frac{\partial \mathcal{L}_{\text{triplet}}}{\partial \mathbf{U}_{n,2}^T} \right|_{\text{spatial}} = \frac{\partial \mathcal{L}_{\text{triplet}}}{\partial \mathbf{O}_{n,2}^T} \dot{\mathbf{h}}(\mathbf{U}_{n,2}^T), \quad (22)$$

Concerning the first LIF neuron layer in the ResBlock:

$$\frac{\partial \mathcal{L}_{\text{triplet}}}{\partial \mathbf{O}_{n,1}^T} = \left. \frac{\partial \mathcal{L}_{\text{triplet}}}{\partial \mathbf{O}_{n,1}^T} \right|_{\text{spatial}} = \frac{\partial \mathcal{L}_{\text{triplet}}}{\partial \mathbf{U}_{n,2}^T} \mathbf{W}_{n,2}, \quad (23)$$

$$\frac{\partial \mathcal{L}_{\text{triplet}}}{\partial \mathbf{U}_{n,1}^T} = \left. \frac{\partial \mathcal{L}_{\text{triplet}}}{\partial \mathbf{U}_{n,1}^T} \right|_{\text{spatial}} = \frac{\partial \mathcal{L}_{\text{triplet}}}{\partial \mathbf{O}_{n,1}^T} \dot{\mathbf{h}}(\mathbf{U}_{n,1}^T). \quad (24)$$

Case 3: At the time $t < T$ and the ResBlock $n = N$. In this case, the derivative depends on both the temporal and spatial domain directions of error propagation. Concerning the second LIF neuron layer in the ResBlock:

$$\begin{aligned} \frac{\partial \mathcal{L}_{\text{triplet}}}{\partial \mathbf{O}_{N,2}^t} &= \left. \frac{\partial \mathcal{L}_{\text{triplet}}}{\partial \mathbf{O}_{N,2}^t} \right|_{\text{spatial}} + \left. \frac{\partial \mathcal{L}_{\text{triplet}}}{\partial \mathbf{O}_{N,2}^t} \right|_{\text{temporal}} \\ &= \text{known values} + \frac{\partial \mathcal{L}_{\text{triplet}}}{\partial \mathbf{U}_{N,2}^{t+1}} \delta_{N,2} \mathbf{U}_{N,2}^t \dot{\mathbf{g}}(\mathbf{O}_{N,2}^t), \end{aligned} \quad (25)$$

$$\begin{aligned} \frac{\partial \mathcal{L}_{\text{triplet}}}{\partial \mathbf{U}_{N,2}^t} &= \left. \frac{\partial \mathcal{L}_{\text{triplet}}}{\partial \mathbf{U}_{N,2}^t} \right|_{\text{spatial}} + \left. \frac{\partial \mathcal{L}_{\text{triplet}}}{\partial \mathbf{U}_{N,2}^t} \right|_{\text{temporal}} \\ &= \frac{\partial \mathcal{L}_{\text{triplet}}}{\partial \mathbf{O}_{N,2}^t} \dot{\mathbf{h}}(\mathbf{U}_{N,2}^t) + \frac{\partial \mathcal{L}_{\text{triplet}}}{\partial \mathbf{U}_{N,2}^{t+1}} \delta_{N,2} \mathbf{g}(\mathbf{O}_{N,2}^t), \end{aligned} \quad (26)$$

Concerning the first LIF neuron layer in the ResBlock:

$$\begin{aligned} \frac{\partial \mathcal{L}_{\text{triplet}}}{\partial \mathbf{O}_{N,1}^t} &= \left. \frac{\partial \mathcal{L}_{\text{triplet}}}{\partial \mathbf{O}_{N,1}^t} \right|_{\text{spatial}} + \left. \frac{\partial \mathcal{L}_{\text{triplet}}}{\partial \mathbf{O}_{N,1}^t} \right|_{\text{temporal}} \\ &= \frac{\partial \mathcal{L}_{\text{triplet}}}{\partial \mathbf{U}_{N,2}^t} \mathbf{W}_{N,2} + \frac{\partial \mathcal{L}_{\text{triplet}}}{\partial \mathbf{U}_{N,1}^{t+1}} \delta_{N,1} \mathbf{U}_{N,1}^t \dot{\mathbf{g}}(\mathbf{O}_{N,1}^t), \end{aligned} \quad (27)$$

$$\begin{aligned} \frac{\partial \mathcal{L}_{\text{triplet}}}{\partial \mathbf{U}_{N,1}^t} &= \left. \frac{\partial \mathcal{L}_{\text{triplet}}}{\partial \mathbf{U}_{N,1}^t} \right|_{\text{spatial}} + \left. \frac{\partial \mathcal{L}_{\text{triplet}}}{\partial \mathbf{U}_{N,1}^t} \right|_{\text{temporal}} \\ &= \frac{\partial \mathcal{L}_{\text{triplet}}}{\partial \mathbf{O}_{N,2}^t} \dot{\mathbf{h}}(\mathbf{U}_{N,1}^t) + \frac{\partial \mathcal{L}_{\text{triplet}}}{\partial \mathbf{U}_{N,1}^{t+1}} \delta_{N,1} \mathbf{g}(\mathbf{O}_{N,1}^t). \end{aligned} \quad (28)$$

Case 4: At the time $t < T$ and the middle ResBlock $n < N$. In this case, the derivative depends on both the temporal and spatial domain directions of error propagation. Concerning the second LIF neuron layer in the ResBlock:

$$\begin{aligned} \frac{\partial \mathcal{L}_{\text{triplet}}}{\partial \mathbf{O}_{n,2}^t} &= \left. \frac{\partial \mathcal{L}_{\text{triplet}}}{\partial \mathbf{O}_{n,2}^t} \right|_{\text{spatial}} + \left. \frac{\partial \mathcal{L}_{\text{triplet}}}{\partial \mathbf{O}_{n,2}^t} \right|_{\text{temporal}} \\ &= \frac{\partial \mathcal{L}_{\text{triplet}}}{\partial \mathbf{U}_{n+1,1}^t} \mathbf{W}_{n,1} + \frac{\partial \mathcal{L}_{\text{triplet}}}{\partial \mathbf{U}_{n+1,2}^t} + \frac{\partial \mathcal{L}_{\text{triplet}}}{\partial \mathbf{U}_{n,2}^{t+1}} \delta_{n,2} \mathbf{U}_{n,2}^t \dot{\mathbf{g}}(\mathbf{O}_{n,2}^t), \end{aligned} \quad (29)$$

$$\begin{aligned} \frac{\partial \mathcal{L}_{\text{triplet}}}{\partial \mathbf{U}_{n,2}^t} &= \left. \frac{\partial \mathcal{L}_{\text{triplet}}}{\partial \mathbf{U}_{n,2}^t} \right|_{\text{spatial}} + \left. \frac{\partial \mathcal{L}_{\text{triplet}}}{\partial \mathbf{U}_{n,2}^t} \right|_{\text{temporal}} \\ &= \frac{\partial \mathcal{L}_{\text{triplet}}}{\partial \mathbf{O}_{n,2}^t} \dot{\mathbf{h}}(\mathbf{U}_{n,2}^t) + \frac{\partial \mathcal{L}_{\text{triplet}}}{\partial \mathbf{U}_{n,2}^{t+1}} \delta_{n,2} \mathbf{g}(\mathbf{O}_{n,2}^t), \end{aligned} \quad (30)$$

Concerning the first LIF neuron layer in the ResBlock:

$$\begin{aligned} \frac{\partial \mathcal{L}_{\text{triplet}}}{\partial \mathbf{O}_{n,1}^t} &= \left. \frac{\partial \mathcal{L}_{\text{triplet}}}{\partial \mathbf{O}_{n,1}^t} \right|_{\text{spatial}} + \left. \frac{\partial \mathcal{L}_{\text{triplet}}}{\partial \mathbf{O}_{n,1}^t} \right|_{\text{temporal}} \\ &= \frac{\partial \mathcal{L}_{\text{triplet}}}{\partial \mathbf{U}_{n,2}^t} \mathbf{W}_{n,2} + \frac{\partial \mathcal{L}_{\text{triplet}}}{\partial \mathbf{U}_{n,1}^{t+1}} \delta_{n,1} \mathbf{U}_{n,1}^t \dot{\mathbf{g}}(\mathbf{O}_{n,1}^t), \end{aligned} \quad (31)$$

$$\begin{aligned} \frac{\partial \mathcal{L}_{\text{triplet}}}{\partial \mathbf{U}_{n,1}^t} &= \left. \frac{\partial \mathcal{L}_{\text{triplet}}}{\partial \mathbf{U}_{n,1}^t} \right|_{\text{spatial}} + \left. \frac{\partial \mathcal{L}_{\text{triplet}}}{\partial \mathbf{U}_{n,1}^t} \right|_{\text{temporal}} \\ &= \frac{\partial \mathcal{L}_{\text{triplet}}}{\partial \mathbf{O}_{n,2}^t} \dot{\mathbf{h}}(\mathbf{U}_{n,1}^t) + \frac{\partial \mathcal{L}_{\text{triplet}}}{\partial \mathbf{U}_{n,1}^{t+1}} \delta_{n,1} \mathbf{g}(\mathbf{O}_{n,1}^t). \end{aligned} \quad (32)$$

Based on the above four cases, we can get the derivative of $\mathcal{L}_{\text{triplet}}$ to $\mathbf{O}_{n,1}^t$, $\mathbf{U}_{n,1}^t$ in the first LIF neuron layer and $\mathbf{O}_{n,2}^t$, $\mathbf{U}_{n,2}^t$ in the second LIF neuron layer at any layer n and any time t , and then get the derivative of $\mathcal{L}_{\text{triplet}}$ to $\mathbf{W}_{n,1}$ in the first LIF neuron layer and $\mathbf{W}_{n,2}$ in the second LIF neuron layer as follows:

$$\frac{\partial \mathcal{L}_{\text{triplet}}}{\partial \mathbf{W}_{n,1}} = \sum_{t=1}^T \frac{\partial \mathcal{L}_{\text{triplet}}}{\partial \mathbf{U}_{n,1}^t} \frac{\partial \mathbf{U}_{n,1}^t}{\partial \mathbf{W}_{n,1}} = \sum_{t=1}^T \frac{\partial \mathcal{L}_{\text{triplet}}}{\partial \mathbf{U}_{n,1}^t} \mathbf{O}_{n-1,2}^t, \quad (33)$$

$$\frac{\partial \mathcal{L}_{\text{triplet}}}{\partial \mathbf{W}_{n,2}} = \sum_{t=1}^T \frac{\partial \mathcal{L}_{\text{triplet}}}{\partial \mathbf{U}_{n,2}^t} \frac{\partial \mathbf{U}_{n,2}^t}{\partial \mathbf{W}_{n,2}} = \sum_{t=1}^T \frac{\partial \mathcal{L}_{\text{triplet}}}{\partial \mathbf{U}_{n,2}^t} \mathbf{O}_{n,1}^t,$$

where $\frac{\partial \mathcal{L}_{\text{triplet}}}{\partial \mathbf{U}_{n,1}^t}$ and $\frac{\partial \mathcal{L}_{\text{triplet}}}{\partial \mathbf{U}_{n,2}^t}$ can be obtained from Eq. (17) to Eq. (32). In spatio-temporal back-propagation, the spike

TABLE I

SCENARIOS, SEQUENCES, TRAINING AND TESTING SETS OF BRISBANE-EVENT-VPR [12] AND DDD20 [46] DATASETS USED IN OUR EXPERIMENTS. THE TEXT IN "{}" INDICATES THE SEQUENCE NAME, AND THE TEXT IN "[]" INDICATES THE NUMBER OF SAMPLES. "&" MEANS TO MERGE SEQUENCES OF TWO SCENES. "/" MEANS TO DISTINGUISH BETWEEN DATABASE AND QUERY. "***" MEANS OMITTED.

Datasets	All Scenarios and Sequences	Experiments	Training Sets (Database / Query)	Testing Sets (Database / Query)
Brisbane-Event-VPR [12]	sunrise (sr) {2020-04-29-06-20-23},	1	(dt & mn) [4712] / sr [2620]	ss1 [1768] / ss2 [1768]
	morning (mn) {2020-04-28-09-14-11},	2	(ss2 & dt) [4002] / mn [2478]	ss1 [2492] / sr [2492]
	daytime (dt) {2020-04-24-15-12-03},	3	(ss2 & dt) [4002] / sr [2620]	ss1 [2478] / mn [2478]
	sunset (ss1, ss2) {2020-04-21-17-03-03, 2020-04-22-17-24-21}	4	(ss2 & mn) [4246] / sr [2620]	ss1 [2181] / dt [2181]
DDD20 [46]	street {rec1501983083, rec1502648048, rec1502325857},	5	***83 [1146] / **57 [1001]	***83 [1146] / ***48 [1146]
	freeway {rec1500924281, rec1501191354, rec1501268968}	6	***81 [5177] / **54 [5583]	***81 [5177] / ***68 [5177]

generating functions $h(\cdot)$ are not differentiable. To facilitate error propagation between neurons, we employ the sigmoid function as a surrogate gradient function to approximate the derivative of $h(\cdot)$, which is presented as follows:

$$\dot{h}(U_n^t) = \frac{1}{\alpha} \cdot \frac{e^{-\frac{U_n^t - u_{th,n}}{\alpha}}}{\left(1 + e^{-\frac{U_n^t - u_{th,n}}{\alpha}}\right)^2}, \quad (34)$$

where $\alpha = 0.25$ and the spike trigger threshold $u_{th,n} = 0.5$. Based on the above principles, we can use gradient descent to train the entire network efficiently.

IV. EXPERIMENTS

In this section, we outline the comprehensive performance of our proposed Spike-EVPR using both quantitative and qualitative results. Firstly, we detail the experimental setup like Dataset Selection, Parameters in Training, Evaluation Metrics, and Baseline Methods in IV-A. Then we compare the performance of our Spike-EVPR with several baseline methods in IV-B. Furthermore, we perform ablation studies on our algorithm, demonstrating the effectiveness of the different modules proposed for the Spike-EVPR in IV-C.

A. Experimental Setup

1) *Dataset Selection*: To assess the performance of our proposed Spike-EVPR, we performed several experiments on the benchmark EVPR datasets, the Brisbane-Event-VPR [12] and DDD20 [46] datasets.

- **Brisbane-Event-VPR**. The Brisbane-Event-VPR [12] dataset comprises data recorded using DAVIS cameras and GPS, capturing six 8km paths at various times of the day. We excluded the night sequence from our evaluation since the camera parameters were not adjusted for challenging lighting conditions. Therefore, we focused on four different sequences: sunrise, morning, daytime, and sunset.
- **DDD20**. The DDD20 [46] dataset is a comprehensive driving dataset captured by event cameras and encompasses various lighting conditions. We specifically chose six sequences from two urban scenes, including two sequences under glare lighting conditions, as well as three sequences involving highway scenarios.

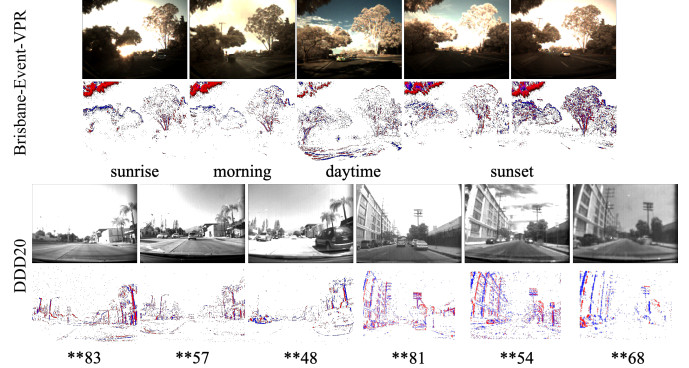


Fig. 5. The Scenarios of Brisbane-Event-VPR [12] and DDD20 [46] datasets in our experiments. Top: event streams and images of the same scene in different illumination periods under different illumination conditions of the Brisbane-Event-VPR Dataset. Bottom: event streams and images of the city/town and freeway scenes for the DDD20 Dataset.

2) *Parameters in Training*: In our training process, we utilize the triplet ranking loss as weakly supervision to train our Spike-EVPR. During training, for query data, we selected one positive sample (within the potential positive distance threshold) and ten negative samples (outside the random negative distance threshold) for triplet metric learning. During testing, for test data, if the image given by the network according to the query event volume is within a 75m radius of the true GPS location, we consider the query to be accurate. We configured the time intervals for the event volumes in the Brisbane-Event-VPR [12] and DDD20 [46] datasets to be approximately 0.25s and 0.2s, respectively. For the event volume time windows in the Brisbane-Event-VPR [12] and DDD20 [46] datasets, we maintained the same settings for the corresponding event streams fragments, used 0.25 seconds and 0.2 seconds, respectively. To ensure a fair comparison across all experiments, we set the learning rate to 0.001, the training batch size to 2, and the cache batch size to 100. For the experiments, we used NVIDIA RTX 4090 for the overall process.

3) *Evaluation Metrics*: We employed Precision-Recall curves and Recall@N, which are widely used evaluation metrics in place recognition [7], [14]. To calculate Recall@N, we followed this procedure: For each query sample, we retrieved the top N nearest neighbors from the database samples based on descriptor distances. If at least one of these retrieved samples was within a geographic distance of less than ϕ (true positive geographic distance threshold) from the query sample, we considered the query sample's location recognition to be

TABLE II
COMPARISON OF OUR SPIKE-EVPR AGAINST EVENT-BASED SOTA VPR METHODS [12] [14] ON BRISBANE-EVENT-VPR [12] AND DDD20 [46] DATASETS WITH THE BEST RESULT **BOLD**ED.

Models	EVPR Methods	Brisbane-Event-VPR [12] Dataset				Avg Recall@1 (%)↑	DDD20 [46] Dataset		
		Recall@1/5 (%)↑					Recall@1/5 (%)↑	F1-max ↑	Avg Recall@1 (%)↑
		F1-max ↑							
ss1 / ss2	ss1 / sr	ss1 / mn	ss1 / dt	ss1 / ss2	ss1 / sr	ss1 / mn	ss1 / dt	**83 / **48	**81 / **68
ANN	Ensemble-Event-VPR [12]	87.33, 95.70	58.82, 82.42	58.42, 78.33	43.62, 62.71	62.05	32.02, 50.17	7.84, 14.99	19.93
	Event-VPR [14] (Ours)	84.79, 93.83	65.65, 86.52	66.67, 84.26	44.54, 66.10	65.41	43.89, 66.67	8.52, 21.33	26.21
	Sparse-Event-VPR [16]	96.35, 98.92	79.41, 92.51	69.76, 87.79	47.13, 69.52	73.16	—	—	—
SNN	Ev-ReconNet [43]	95.73, 98.26	66.08, 86.72	44.60, 66.70	36.37, 58.33	60.70	—	—	—
	Spike-EVPR (Ours)	87.78, 96.04	86.56, 95.27	88.98, 96.33	59.77, 79.45	80.77	58.12, 79.76	20.69, 37.07	39.41

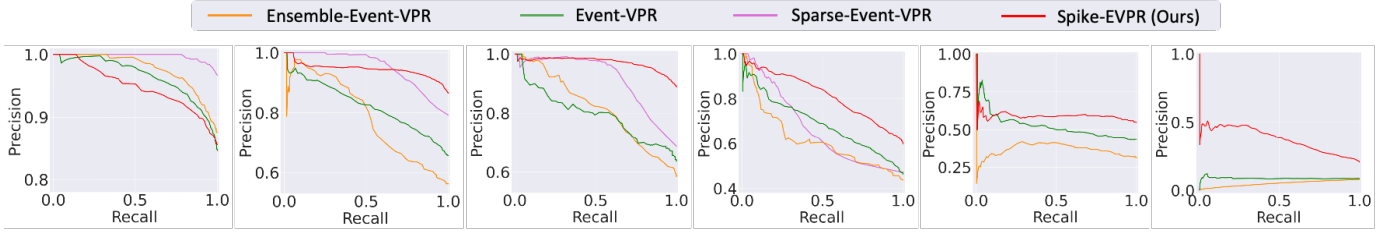


Fig. 6. PR curves of Ensemble-Event-VPR [12], Event-VPR (ours) [14], Sparse-Event-VPR [16], and Spike-EVPR (ours) on Brisbane-Event-VPR [12] and DDD20 [46] datasets. The first four subgraphs are on Brisbane-Event-VPR [12], and the last two subgraphs are on DDD20 [46]. Our Spike-EVPR (red) performs better than SOTA EVPR methods under most scenes.

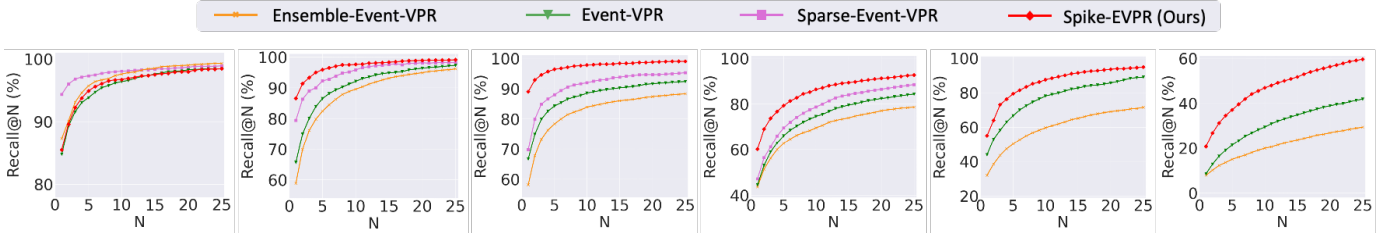


Fig. 7. Recall@N curves of Ensemble-Event-VPR [12], Event-VPR (ours) [14], Sparse-Event-VPR [16], and Spike-EVPR (ours) on Brisbane-Event-VPR [12] and DDD20 [46] datasets. The first four subgraphs are on Brisbane-Event-VPR [12], and the last two subgraphs are on DDD20 [46]. Our Spike-EVPR (red) performs better than SOTA EVPR methods under most scenes. The “N” in the horizontal axis means “number of top database candidates”.

correct. We then plotted the Recall@N curve to analyze the performance across different N values. In our experiments, we focused on $N = 1, 5, 10, 20$ for analysis. We also calculate F1-max for a more comprehensive comparison (see [7], [14] for details).

4) *Baseline Methods*: We demonstrate the outstanding performance of our proposed Spike-EVPR by comparing it with several SOTA EVPR methods such as Ensemble-Event-VPR [12], Event-VPR [14], Sparse-Event-VPR [16], and Ev-ReconNet [43]. Among them, both Ensemble-Event-VPR and Ev-ReconNet rely on the reconstruction of event edge images, and then use NetVLAD to construct global descriptors. The difference between them is that the reconstruction of Ensemble-Event-VPR is based on the ANN but the reconstruction of Ev-ReconNet is based on the SNN. We also compared it with our previous work, Event-VPR, which first processes the event volume as Event Spike Tensor (EST), uses the ResNet to extract features, and finally uses NetVLAD for feature aggregation.

B. Comparison against SOTA Methods

1) *Comparison against ANN-based EVPR Methods*: Here, we compare the proposed Spike-EVPR with ANN-based EVPR SOTA methods, including Ensemble-Event-VPR [12], Event-VPR [14], and Sparse-Event-VPR [16]. As shown in Table II, our method outperforms the above EVPR pipelines in most cases on the Brisbane-Event-VPR and DDD20 datasets. Compared to the Sparse-Event-VPR, the Recall@1 of our Spike-EVPR is 7.15%, 19.22%, and 12.64% higher on ss1/sr, ss1/mn and ss1/dt of the Brisbane-Event-VPR dataset, respectively. As a whole, the Recall@1 of our Spike-EVPR is 7.61% higher than that of Sparse-Event-VPR on average. On the DDD20 dataset, the Recall@1 of our Spike-EVPR are 19.48% and 13.20% higher than those of Ensemble-Event-VPR and Event-VPR on average, respectively. In addition, the PR curves in Fig. 6 also illustrate that our Spike-EVPR achieves better results than other baseline methods. These qualitative results also illustrate that our Spike-EVPR can achieve better place recognition performance than other methods. Due to introducing cross-representation aggregation, our Spike-EVPR can adequately capture more temporal and spatial information about the scene. Meanwhile, our Spike-EVPR uses SSD-

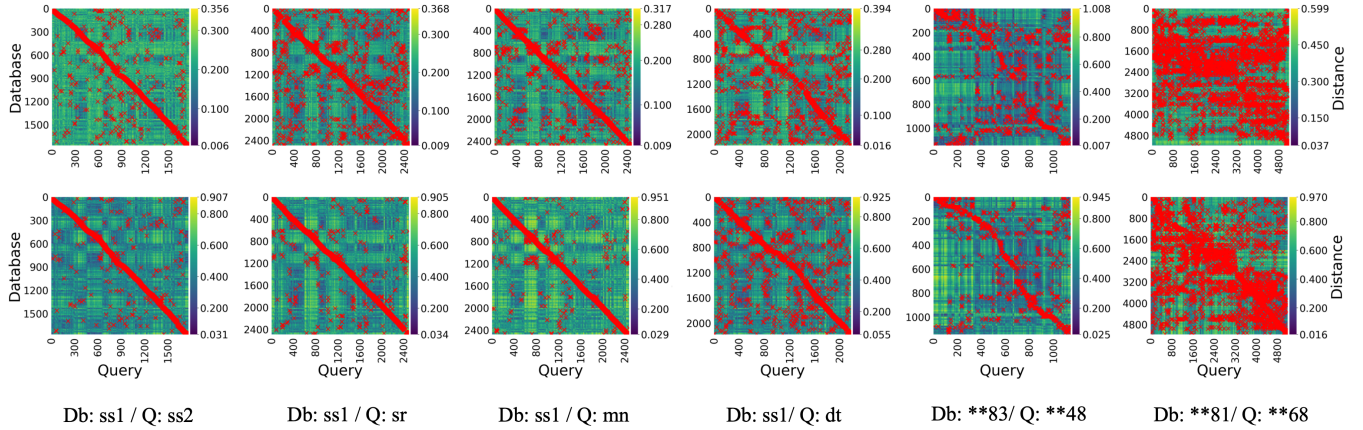


Fig. 8. Matching Matrices between Databases and Queries of Event-VPR [14] and our Spike-EVPR on Different Illumination Sequences on Brisbane-Event-VPR [12] and DDD20 [46] datasets. The first four subgraphs are on Brisbane-Event-VPR [12], and the last two subgraphs are on DDD20 [46]. Top: Event-VPR [14], bottom: Spike-EVPR (ours). The red cross represents the descriptor-matching result of query samples and database samples. The more red cross is concentrated on the diagonal, the better the performance. The background shows the descriptor distance matrix between all query samples and all database samples. (Note: Here 'Db' and 'Q' mean 'Database' and 'Query' respectively.)

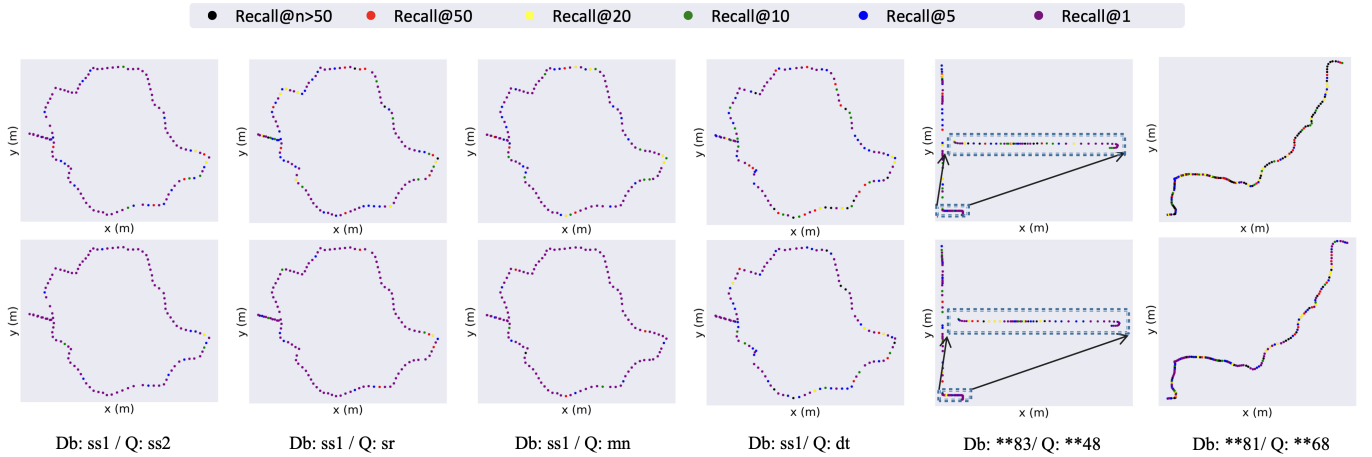


Fig. 9. Retrieval Success-Rate Maps between Databases and Queries of Event-VPR [14] and our Spike-EVPR on Brisbane-Event-VPR [12] and DDD20 [46] datasets. The first four subgraphs are on Brisbane-Event-VPR [12], and the last two subgraphs are on DDD20 [46]. Top: Event-VPR [14], bottom: Spike-EVPR (ours).

Extractor to discover shared and specific features between different spike representations and introduces CDA-Module to learn the weights between different features to derive a more robust scene descriptor. Therefore, as shown in Table II and Fig. 7, our Spike-EVPR can achieve SOTA performance with cross-representation aggregation using deep spiking residual networks. As a supplement, the distance matrix and retrieval success rate maps of our algorithm against Event-VPR are shown in Fig. 8 and Fig. 9.

2) *Comparison against SNN-based EVPR Method:* At present, Ev-ReconNet [43] is the only method which utilize SNNs for EVPR. This method solely employs SNNs for reconstructing event edge images from the event streams. However, the feature extraction part adopts the well-established NetVLAD method. Therefore, this method does not take full advantage of the ability of SNNs to extract the spatiotemporal features of event streams. On the contrary, our proposed Spike-EVPR is designed as an end-to-end EVPR network that utilizes SNNs to extract spatiotemporal features. Experimental results show that the Recall@1 of our Spike-EVPR is 20.07% higher than that of Ev-ReconNet on average. The reason for the gap in performance on the ss1/ss2 sequence may be that

the illumination conditions of the database and query on this sequence are almost the same, and the Ev-ReconNet based on the event edge image reconstruction can reconstruct superior quality and similar images so that their effect on this sequence is better than ours.

C. Ablation Studies

In this section, we explore the impact of BSR-Encoder, SSD-Extractor, and CDA-Module on the performance of our Spike-EVPR using the Brisbane-Event-VPR [12] and DDD20 [46] datasets. The experimental results are shown in Table III.

1) *Impact of BSR-Encoder:* BSR-Encoder is only a feature encoding network, and the main discussion in this section is the influence of the proposed two event spike representations on EVPR. In this experiment, we discard the proposed SSD-Extractor and CDA-Module and only remain the BSR-Encoder. For using a single spike representation experiment, we directly use global average pooling and L2 Normalization to get the final global descriptor. For using both representations, after global average pooling and L2 Normalization operation, we add the two descriptors together as the final

TABLE III
ABLATION STUDIES ON THE IMPACT OF DIFFERENT MODULES ON THE PERFORMANCE OF OUR SPIKE-EVPR WITH THE BEST RESULTS BOLDED.

Ablation Studies	Settings	Recall@1/5 (%)									
		Brisbane-Event-VPR [12] Dataset					DDD20 [46] Dataset				
		ss1 / ss2	ss1 / sr	ss1 / mn	ss1 / dt	**83 / **48	**81 / **68				
BSR-Encoder	Only MCS-Tensor Encoder	74.21, 84.36	73.39, 82.49	76.36, 84.67	49.17, 70.54	42.79, 67.12	13.44, 30.85				
	Only TSS-Tensor Encoder	77.74, 87.31	75.13, 84.92	77.81, 85.33	51.69, 71.37	45.63, 68.79	14.12, 30.39				
	MCS-Tensor & TSS-Tensor Encoder	82.13, 91.43	80.99, 91.62	81.32, 90.91	53.42, 72.33	50.17, 70.01	16.54, 32.94				
SSD-Extractor	Without SSD-Extractor	85.10, 91.25	84.80, 94.15	86.80, 95.20	56.38, 76.10	52.73, 72.45	18.11, 34.55				
	With SSD-Extractor	87.78, 96.04	86.56, 95.87	88.98, 96.33	59.77, 79.45	58.12, 79.76	21.48, 37.16				
CDA-Module	Directly concat without CDA-Module	83.66, 93.46	84.12, 94.33	84.23, 92.04	56.12, 76.88	55.61, 74.74	18.76, 36.76				
	Addition replace flatten	86.31, 94.23	84.87, 94.67	87.89, 94.88	57.61, 77.11	56.11, 77.39	19.76, 36.76				
	Concat with CDA-Module	87.78, 96.04	86.56, 95.87	88.98, 96.33	59.77, 79.45	58.12, 79.76	21.48, 37.16				

global descriptor. The experiment in Table III demonstrates that using a single type of spike representation leads to severe performance degradation on both datasets. Moreover, the SOTA performance of our Spike-EVPR is attributed to using the two spike representations simultaneously rather than a single type of spike representation.

2) *Impact of SSD-Extractor*: In this experiment, we excluded the SSD-Extractor network module. After the BSR-Encoder, we conduct the two feature maps through global average pooling and L2 normalization to get two descriptors as inputs for the CDA-Module network module. At the same time, we need to modify the output of the SNN-MLP within the CDA-Module to 2. The comparison results in Table III show that the performance of our network can be further enhanced with SSD-Extractor. In more detail, the introduction of the shared and specific extraction exhibits an average Recall@1 increase of 3.10%, with a notable increase of 4.68% in SS1/SS2. For the DDD20 dataset, there is an average recall@1 improvement of 4.38%. These results demonstrate that the shared and specific features could introduce more information and enhance the ability of our Spike-EVPR to generate a more robust scene descriptor.

3) *Impact of CDA-Module*: To comprehensively validate the impact of the CDA-Module on Spike-EVPR, we implemented the following configurations for the ablation study: (1) Directly concatenating the specific and shared descriptors generated by the SSD-Extractor in the final dimension, bypassing the CDA-Module module. (2) Replacing the flatten operation in CDA-Module with an addition operation. (3) Using the proposed CDA-Module. The improved Recall@1 values demonstrate that CDA-Module effectively learns the weights of specific and shared descriptors' contributions to the final descriptor. This enables the final descriptor to encapsulate richer feature information and prioritize the features that significantly contribute to the robust representation ability, akin to attention mechanisms.

4) *Algorithm Performance under Different True Positive Geographic Distance Thresholds*: To comprehensively evaluate the performance of our Spike-EVPR pipeline, this section presents its performance across a range of true positive geographic distance thresholds ϕ , specifically focusing on the Recall@1 values. The results are presented in Table IV and Fig. 10. It is evident that as the true positive geographic distance threshold ϕ decreases, the Recall@1 value also gradually

decreases. Nonetheless, even at a true positive geographic distance threshold of only 30m, our Spike-EVPR demonstrates strong performance. The decline in performance from 75m to 30m is not particularly significant. However, a more substantial decrease in performance is observed when the true positive geographic distance threshold is reduced from 30m to 15m. This can likely be attributed to some GPS data having a sampling frequency exceeding 2s and average vehicle speeds from 10m/s to 15m/s, resulting in a few adjacent GPS data points having distances greater than 15m. This can lead to inaccurate matching.

TABLE IV
PERFORMANCE EVALUATION FOR OUR SPIKE-EVPR UNDER DIFFERENT TRUE POSITIVE GEOGRAPHIC DISTANCE THRESHOLD ϕ .

Geographic Threshold ϕ	Recall@1 (%)					
	Brisbane-Event-VPR [12] Dataset			DDD20 [46] Dataset		
	ss1 / ss2	ss1 / sr	ss1 / mn	ss1 / dt	**83 / **48	**81 / **68
15m	75.28	76.21	79.06	43.21	44.94	6.05
30m	86.09	84.64	86.40	55.32	50.79	14.24
45m	87.05	85.84	87.69	57.98	53.40	17.79
60m	87.44	86.16	88.30	58.85	55.85	19.63
75m	87.78	86.56	88.98	59.77	58.12	21.48

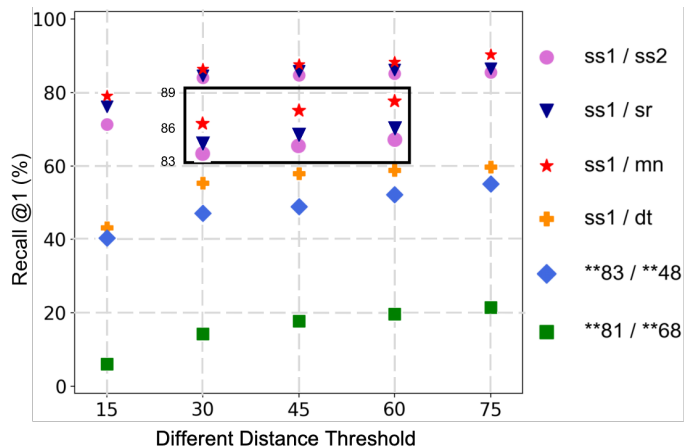


Fig. 10. Performance evaluation under different true positive geographic distance threshold on Brisbane-Event-VPR [12] and DDD20 [46] datasets.

V. CONCLUSIONS

In this article, we analyze the challenges in utilizing SNNs for event data processing in EVPR from the perspective of

event spike representation and network architecture. Based on that, we propose a method for event-based visual place recognition with cross-representation aggregation based on the deep spiking residual network (Spike-EVPR). The two key ideas of our EV-MGRFlowNet are as follows: First, we design two event spike representations fitted for SNNs to capture the temporal and spatial information of event streams comprehensively. Additionally, we design a robust spike feature extraction network pipeline composed of BSR-Encoder, SSD-Extractor, and CDA-Module to extract event features and aggregate global descriptors of the scene effectively. Hence, our proposed pipeline unlocks the potential to use SNNs to process event volume and build global descriptors. Comparisons with existing SOTA ANN-based EVPR methods reveal that Spike-EVPR consistently achieves superior performance. Additionally, when compared with the existing SNN-based EVPR method, our approach excels across various scenarios. Looking ahead, our future work will focus on optimizing the network pipeline for lightweight deployment and accelerated performance on self-driving cars or mini drones. Furthermore, we aim to explore the deployment of our pipeline on neuromorphic chips to enable energy-efficient inference [47], [48].

REFERENCES

- [1] G. Gallego, T. Delbrück, G. Orchard, C. Bartolozzi, B. Taba, A. Censi, S. Leutenegger, A. J. Davison, J. Conradt, K. Daniilidis *et al.*, “Event-based vision: A survey,” *IEEE transactions on pattern analysis and machine intelligence*, vol. 44, no. 1, pp. 154–180, 2020.
- [2] G. Chen, H. Cao, J. Conradt, H. Tang, F. Rohrbein, and A. Knoll, “Event-based neuromorphic vision for autonomous driving: A paradigm shift for bio-inspired visual sensing and perception,” *IEEE Signal Processing Magazine*, vol. 37, no. 4, pp. 34–49, 2020.
- [3] X. Zheng, Y. Liu, Y. Lu, T. Hua, T. Pan, W. Zhang, D. Tao, and L. Wang, “Deep learning for event-based vision: A comprehensive survey and benchmarks,” *arXiv preprint arXiv:2302.08890*, 2023.
- [4] H. Zhuang, X. Huang, K. Hou, D. Kong, C. Hu, and Z. Fang, “Ev-mgrflownet: Motion-guided recurrent network for unsupervised event-based optical flow with hybrid motion-compensation loss,” *arXiv preprint arXiv:2305.07853*, 2023.
- [5] T.-H. Wu, C. Gong, D. Kong, S. Xu, and Q. Liu, “A novel visual object detection and distance estimation method for hdr scenes based on event camera,” in *International Conference on Computer and Communications*, 2021, pp. 636–640.
- [6] L. Pan, C. Scheerlinck, X. Yu, R. Hartley, M. Liu, and Y. Dai, “Bringing a blurry frame alive at high frame-rate with an event camera,” in *Proceedings of the IEEE/CVF Conference on Computer Vision and Pattern Recognition*, 2019, pp. 6820–6829.
- [7] K. Hou, D. Kong, J. Jiang, H. Zhuang, X. Huang, and Z. Fang, “Fusion-vpr: Attention-based multi-scale network architecture for visual place recognition by fusing frames and events,” *IEEE Robotics and Automation Letters*, 2023.
- [8] S. Lowry, N. Sünderhauf, P. Newman, J. J. Leonard, D. Cox, P. Corke, and M. J. Milford, “Visual place recognition: A survey,” *IEEE transactions on robotics*, vol. 32, no. 1, pp. 1–19, 2015.
- [9] X. Zhang, L. Wang, and Y. Su, “Visual place recognition: A survey from deep learning perspective,” *Pattern Recognition*, vol. 113, p. 107760, 2021.
- [10] C. Masone and B. Caputo, “A survey on deep visual place recognition,” *IEEE Access*, vol. 9, pp. 19 516–19 547, 2021.
- [11] S. Garg, T. Fischer, and M. Milford, “Where is your place, visual place recognition?” *arXiv preprint arXiv:2103.06443*, 2021.
- [12] T. Fischer and M. Milford, “Event-based visual place recognition with ensembles of temporal windows,” *IEEE Robotics and Automation Letters*, vol. 5, no. 4, pp. 6924–6931, 2020.
- [13] A. J. Lee and A. Kim, “Eventvlad: Visual place recognition with reconstructed edges from event cameras,” in *IEEE/RSJ International Conference on Intelligent Robots and Systems*, 2021, pp. 2247–2252.
- [14] D. Kong, Z. Fang, K. Hou, H. Li, J. Jiang, S. Coleman, and D. Kerr, “Event-vpr: End-to-end weakly supervised deep network architecture for visual place recognition using event-based vision sensor,” *IEEE Transactions on Instrumentation and Measurement*, vol. 71, pp. 1–18, 2022.
- [15] Z. Huang, R. Huang, L. Sun, C. Zhao, M. Huang, and S. Su, “Vefnet: an event-rgb cross modality fusion network for visual place recognition,” in *IEEE International Conference on Image Processing*, 2022, pp. 2671–2675.
- [16] T. Fischer and M. Milford, “How many events do you need? event-based visual place recognition using sparse but varying pixels,” *IEEE Robotics and Automation Letters*, vol. 7, no. 4, pp. 12 275–12 282, 2022.
- [17] K. Roy, A. Jaiswal, and P. Panda, “Towards spike-based machine intelligence with neuromorphic computing,” *Nature*, vol. 575, no. 7784, pp. 607–617, 2019.
- [18] W. Maass, “Networks of spiking neurons: the third generation of neural network models,” *Neural networks*, vol. 10, no. 9, pp. 1659–1671, 1997.
- [19] R. Massa, A. Marchisio, M. Martina, and M. Shafique, “An efficient spiking neural network for recognizing gestures with a dvs camera on the loihi neuromorphic processor,” in *2020 International Joint Conference on Neural Networks (IJCNN)*. IEEE, 2020, pp. 1–9.
- [20] Y. Xing, G. Di Caterina, and J. Soraghan, “A new spiking convolutional recurrent neural network (scrnn) with applications to event-based hand gesture recognition,” *Frontiers in neuroscience*, vol. 14, p. 590164, 2020.
- [21] D. G. Lowe, “Distinctive image features from scale-invariant keypoints,” *International journal of computer vision*, vol. 60, no. 2, pp. 91–110, 2004.
- [22] A. Angeli, D. Filliat, S. Doncieux, and J.-A. Meyer, “Fast and incremental method for loop-closure detection using bags of visual words,” *IEEE transactions on robotics*, vol. 24, no. 5, pp. 1027–1037, 2008.
- [23] E. Rublee, V. Rabaud, K. Konolige, and G. Bradski, “Orb: An efficient alternative to sift or surf,” in *International conference on computer vision*, 2011, pp. 2564–2571.
- [24] D. Gálvez-López and J. D. Tardos, “Bags of binary words for fast place recognition in image sequences,” *IEEE Transactions on Robotics*, vol. 28, no. 5, pp. 1188–1197, 2012.
- [25] R. Arandjelovic, P. Gronat, A. Torii, T. Pajdla, and J. Sivic, “Netvlad: Cnn architecture for weakly supervised place recognition,” in *IEEE conference on computer vision and pattern recognition*, 2016, pp. 5297–5307.
- [26] H. Jégou, M. Douze, C. Schmid, and P. Pérez, “Aggregating local descriptors into a compact image representation,” in *IEEE computer society conference on computer vision and pattern recognition*, 2010, pp. 3304–3311.
- [27] J. Yu, C. Zhu, J. Zhang, Q. Huang, and D. Tao, “Spatial pyramid-enhanced netvlad with weighted triplet loss for place recognition,” *IEEE transactions on neural networks and learning systems*, vol. 31, no. 2, pp. 661–674, 2019.
- [28] S. Hausler, S. Garg, M. Xu, M. Milford, and T. Fischer, “Patch-netvlad: Multi-scale fusion of locally-global descriptors for place recognition,” in *IEEE/CVF Conference on Computer Vision and Pattern Recognition*, 2021, pp. 14 141–14 152.
- [29] G. Berton, C. Masone, and B. Caputo, “Rethinking visual geo-localization for large-scale applications,” in *Proceedings of the IEEE/CVF Conference on Computer Vision and Pattern Recognition*, 2022, pp. 4878–4888.
- [30] A. Ali-Bey, B. Chaib-Draa, and P. Giguere, “Mixvpr: Feature mixing for visual place recognition,” in *Proceedings of the IEEE/CVF Winter Conference on Applications of Computer Vision*, 2023, pp. 2998–3007.
- [31] A. Ali-bey, B. Chaib-draa, and P. Giguère, “Gsv-cities: Toward appropriate supervised visual place recognition,” *Neurocomputing*, vol. 513, pp. 194–203, 2022.
- [32] N. Keetha, A. Mishra, J. Karhade, K. M. Jatavallabhula, S. Scherer, M. Krishna, and S. Garg, “Anyloc: Towards universal visual place recognition,” *IEEE Robotics and Automation Letters*, 2023.
- [33] M. Oquab, T. Darcet, T. Moutakanni, H. Vo, M. Szafraniec, V. Khalidov, P. Fernandez, D. Haziza, F. Massa, A. El-Nouby *et al.*, “Dinov2: Learning robust visual features without supervision,” *arXiv preprint arXiv:2304.07193*, 2023.
- [34] E. Hunsberger and C. Eliasmith, “Spiking deep networks with lif neurons,” *arXiv preprint arXiv:1510.08829*, 2015.
- [35] B. Rueckauer, I.-A. Lungu, Y. Hu, M. Pfeiffer, and S.-C. Liu, “Conversion of continuous-valued deep networks to efficient event-driven networks for image classification,” *Frontiers in neuroscience*, vol. 11, p. 682, 2017.

- [36] B. Han and K. Roy, "Deep spiking neural network: Energy efficiency through time based coding," in *European Conference on Computer Vision*. Springer, 2020, pp. 388–404.
- [37] S. Deng and S. Gu, "Optimal conversion of conventional artificial neural networks to spiking neural networks," *arXiv preprint arXiv:2103.00476*, 2021.
- [38] E. O. Neftci, H. Mostafa, and F. Zenke, "Surrogate gradient learning in spiking neural networks: Bringing the power of gradient-based optimization to spiking neural networks," *IEEE Signal Processing Magazine*, vol. 36, no. 6, pp. 51–63, 2019.
- [39] F. Yang, L. Su, J. Zhao, X. Chen, X. Wang, N. Jiang, and Q. Hu, "Saflo-net: Event-based self-attention optical flow estimation with spiking-analogue neural networks," *IET Computer Vision*, 2023.
- [40] C. M. Parameshwara, S. Li, C. Fermüller, N. J. Sanket, M. S. Evanusa, and Y. Aloimonos, "Spikems: Deep spiking neural network for motion segmentation," in *2021 IEEE/RSJ International Conference on Intelligent Robots and Systems (IROS)*. IEEE, 2021, pp. 3414–3420.
- [41] F. Gu, W. Sng, T. Taunyazov, and H. Soh, "Tactilesnet: A spiking graph neural network for event-based tactile object recognition," in *2020 IEEE/RSJ International Conference on Intelligent Robots and Systems (IROS)*. IEEE, 2020, pp. 9876–9882.
- [42] X. Wu, W. He, M. Yao, Z. Zhang, Y. Wang, and G. Li, "Mss-depthnet: Depth prediction with multi-step spiking neural network," *arXiv preprint arXiv:2211.12156*, 2022.
- [43] H. Lee and H. Hwang, "Ev-reconnet: Visual place recognition using event camera with spiking neural networks," *IEEE Sensors Journal*, 2023.
- [44] A. N. Burkitt, "A review of the integrate-and-fire neuron model: I. homogeneous synaptic input," *Biological cybernetics*, vol. 95, pp. 1–19, 2006.
- [45] X. Lagorce, G. Orchard, F. Galluppi, B. E. Shi, and R. B. Benosman, "Hots: a hierarchy of event-based time-surfaces for pattern recognition," *IEEE transactions on pattern analysis and machine intelligence*, vol. 39, no. 7, pp. 1346–1359, 2016.
- [46] Y. Hu, J. Binas, D. Neil, S.-C. Liu, and T. Delbruck, "Ddd20 end-to-end event camera driving dataset: Fusing frames and events with deep learning for improved steering prediction," in *International Conference on Intelligent Transportation Systems*, 2020, pp. 1–6.
- [47] J. Jiang, D. Kong, K. Hou, X. Huang, H. Zhuang, and Z. Fang, "Neuro-planner: A 3d visual navigation method for mav with depth camera based on neuromorphic reinforcement learning," *IEEE Transactions on Vehicular Technology*, vol. 72, no. 10, pp. 12 697–12 712, 2023.
- [48] F. Yu, Y. Wu, S. Ma, M. Xu, H. Li, H. Qu, C. Song, T. Wang, R. Zhao, and L. Shi, "Brain-inspired multimodal hybrid neural network for robot place recognition," *Science Robotics*, vol. 8, no. 78, p. eabm6996, 2023.



Chenming Hu received the B.S. degree in robot engineering from Nanjing University of Information Science and Technology, Nanjing, China, in 2022. He is currently pursuing the M.S. degree in robot science and engineering with Northeastern University, Shenyang, China. His research interests include event-based vision, deep learning, and neuromorphic computing.



Zheng Fang (Member, IEEE) received the B.S. degree in automation and a Ph.D. degree in pattern recognition and intelligent systems from Northeastern University, Shenyang, China, in 2002 and 2006, respectively. He was a Post-Doctoral Research Fellow at the Robotics Institute of Carnegie Mellon University (CMU), Pittsburgh, PA, USA, from 2013 to 2015. He is currently a full Professor with the Faculty of Robot Science and Engineering, Northeastern University. He has published over 80 papers in well-known journals or conferences in robotics

and computer vision. His research interests include visual/laser simultaneous localization and mapping (SLAM), and perception and autonomous navigation of various mobile robots.



Kuanxu Hou received the B.S. degree in robot engineering and the M.S. degree in robot science and engineering from Northeastern University, Shenyang, China, in 2020 and 2023. Since 2023, he has worked as a robot algorithm engineer at Contemporary Amperex Technology Co., Limited. He also has been a Research Assistant at Northeastern University. His research interests include event-based vision, visual place recognition, and neuromorphic computing.



Delei Kong (Graduate Student Member, IEEE) received the B.S. degree in automation from Henan Polytechnic University, Zhengzhou, China, in 2018 and the M.S. degree in control engineering from Northeastern University, Shenyang, China, in 2021. From 2020 to 2021, he worked as an Algorithm Intern at SynSense Tech. Co. Ltd. From 2021 to 2022, he worked as an R&D Engineer (advanced vision) at Machine Intelligence Laboratory, China Nanhu Academy of Electronics and Information Technology (CNAEIT). Since 2021, he also has been a Research Assistant at Northeastern University. His research interests include event-based vision, robot visual navigation, and neuromorphic computing.



Junjie Jiang received the B.S. degree in automation from Northeastern University at Qinhuangdao, Qinhuangdao, China, in 2020 and the M.S. degree in robot science and engineering from Northeastern University, Shenyang, China, in 2023. He is currently pursuing the Ph.D. degree in robot science and engineering with Northeastern University, Shenyang, China. His research interests include spiking neural network, robot visual navigation, and reinforcement learning.



Hao Zhuang received the B.S. degree in mechanical and electronic engineering with Chongqing University of Posts and Telecommunications, Chongqing, China, in 2021. He is currently pursuing the M.S. degree in control engineering with Northeastern University, Shenyang, China. His research interests include event-based vision, optical flow estimation, and deep learning.



Mingyuan Sun received the B.S. degree in robot engineering from Northeastern University, Shenyang, China, in 2022. He is currently pursuing the M.S. degree in robot science and engineering with Northeastern University, Shenyang, China. His research interests include event-based vision, deep learning and neuromorphic computing.



Xinjie Huang received the B.S. degree in automation with Zhejiang University of Technology, Hangzhou, China, in 2021. He is currently pursuing the M.S. degree in robot science and engineering with Northeastern University, Shenyang, China. His research interests include event-based vision, depth estimation, and deep learning.